IEEE Access
Multidisciplinary | Rapid Review | Open Access Journal

Received 2 May 2024, accepted 10 May 2024, date of publication 14 May 2024, date of current version 21 May 2024.

*Digital Object Identifier 10.1109/ACCESS.2024.3401021*

RESEARCH ARTICLE

# Enhanced Precision in Beam Pattern Synthesis for Compact Transmitarray Antenna Design: Integrating Comprehensive Unit Cell and Measurement Environment Models

**MYEONGHA HWANG[1], GYOUNGDEUK KIM[1], INGON LEE[2], SANGKIL KIM[1], (Senior Member, IEEE), AND JONG-GWAN YOOK[3], (Senior Member, IEEE)**

[1]Department of Electronics Engineering, Pusan National University, Busan 46241, Republic of Korea
[2]Hanwha Systems, Yongin 17121, Republic of Korea
[3]Department of Electrical and electronics Engineering, Yonsei University, Seoul 03722, Republic of Korea

Corresponding author: Sangkil Kim (ksangkil3@pusan.ac.kr)

This work was supported by the Grant-in-Aid of Hanwha Systems based on the Challenging Future Defense Technology Research and Development Program of the Agency for Defense Development in 2019 under Grant 9127786.

**ABSTRACT** This study introduces a high-accuracy beam pattern synthesis technique using comprehensive unit cell and near-field measurement environment modeling for a miniaturized 8 × 8 transmitarray antenna with a unit cell period of $0.4\lambda_0$. The unit cell comprises transmitting and receiving antennas, a single pole double throw PIN diode switch, and a two-stage reflection-type phase shifter. This beam pattern synthesis methodology integrates measured data from individual unit cell components, coupled with simulations of a simple feed antenna and an infinite array transmitting antenna. This approach enables precise prediction of the transmitarray's beam pattern and overall performance, effectively circumventing the need for extensive finite array full-wave electromagnetic simulations. Notably, the calculated beam pattern closely aligns with the experimental results with high accuracy.

**INDEX TERMS** Transmitarray antenna, beam pattern synthesis, reconfigurable antenna, array factor, near-field measurement.

## I. INTRODUCTION

In recent years, there has been a noticeable increase in interest in smart antennas for the next generation of communication and radar systems. These antennas offer the potential to enable high data rates in RF front-end systems with limited form factors, such as small satellites and unmanned aerial vehicles (UAVs). The implementation of such smart antenna systems becomes pivotal in meeting the ever-increasing demands of modern communication requirements. Among the essential demands, beam steering capabilities play a crucial role in ensuring efficient communication. Conventional active phased array antennas have been widely adopted to achieve high-performance beam steering or forming functions, but they require complex feeding networks, high power consumption, high-cost transceiver modules, etc. As a result, transmitarray and reflectarray antennas have attracted significant attention in the last decade due to their relatively simple structures, low-power consumption, and multi-functional beam control capabilities. For example, these antennas could be utilized in conjunction with reconfigurable intelligent surface (RIS) systems or origami theory to enable new applications [1], [2], [3], [4], [5].

Designing and validating array antennas demands meticulous consideration of numerous factors. Consequently, predicting the performance of the array antenna during the design phase is important to minimize the costly and

The associate editor coordinating the review of this manuscript and approving it for publication was Shah Nawaz Burokur.

time-consuming optimization process in the validation stage. High-frequency electromagnetic (EM) simulation tools offer an effective method for anticipating final measurement results and analyzing potential issues. Nevertheless, for antenna arrays, simulating the entire system by accounting for the performance of every element becomes increasingly challenging due to the large number of circuits required for antenna operation and the complexity of modeling nonlinear components. This demands substantial computing power as well as leads to an exponential increase in simulation time. For large arrays, analyzing the antenna array through finite array EM simulation by accounting for every single element would be intractable. In most cases, the array factor (AF) analysis-based beam pattern synthesis method, which is grounded in array theory, is widely adopted to predict the characteristics of the antenna array and analyze its performance. Because it assumes direct feeding to each array element, this method is well-suited for analyzing phased arrays.

On the other hand, since transmit- and reflect-arrays are fed by feed antennas, it is crucial to consider the feed environment. Due to their structural similarities, the theoretical methods for synthesizing transmitarray beam patterns share similarities with the well-established beam synthesis approaches used for reflectarrays. Reflectarrays typically employ two main methodologies for beam synthesis: the array theory approach and the aperture field approach [6], [7]. Likewise, transmitarrays frequently adopt these methodologies for beam formulation, as reported in [8] and [9]. Alternative theoretical beam synthesis methodologies have explored strategies such as geometrical optics [10], near-field synthesis via FFT [11], and the generalized intersection method [12]. However, these methodologies reported so far exhibit inherent limitations in accurately predicting beam patterns due to the challenges of comprehensively incorporating both the characteristics of the complex-configured unit cell elements and the measurement environment. Inaccurately modeling the actual antenna array's characteristics or inadequately accounting for measurement losses can introduce unknown errors, which in turn increase uncertainty in the predicted beam patterns. This can hinder the analysis and improvement of the fabricated array antenna without resorting to finite array EM simulation. As a consequence of these difficulties, the reported papers [13], [14], [15], [16], [17], [18] have employed normalized gain patterns instead of unnormalized gain patterns when comparing measured results with simulation values.

This paper introduces an efficient design and analysis method for transmitarray antenna through high accuracy array modeling using simple simulations, such as single antenna and finite array simulations, and unit cell measurement data without any finite array antenna EM simulation. The proposed beam pattern synthesis method enhances the capabilities of AF analysis-based methods by incorporating the actual near-field measurement environment and the element characteristics of the unit cell. This enables not only the prediction of optimized measurement results quantitatively but also the accurate analysis of the measured array antenna without requiring finite array EM simulations. This approach simplifies the design workflow, fostering a more time- and cost-effective approach to array antenna design.

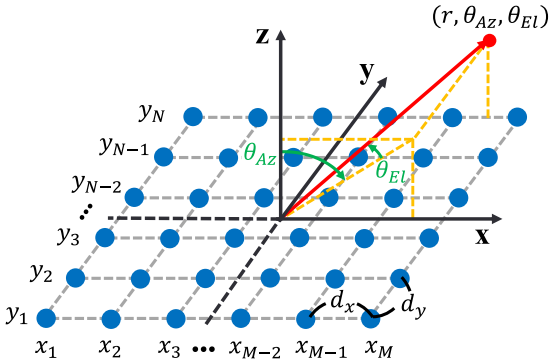


**FIGURE 1.** Two-dimensional uniform antenna element distribution.

The organization of this paper is as follows. Section II describes the beam pattern synthesis method and the parameters incorporated in the beam pattern calculation for the design of the transmitarray antenna, considering the near-field measurement environment. Section III presents the design and measurement of unit cells, as well as the simulation of the feeding antenna, to apply data to the parameters. Section IV shows the optimized measurement cases and analysis of the fabricated transmitarray antenna measurement results through the proposed beam pattern synthesis. Finally, Section V concludes the research.

## II. BEAM PATTERN SYNTHESIS WITH HIGH-ACCURACY ANTENNA ARRAY MODELING

Beam pattern synthesis for transmitarray antenna starts with AF analysis as with conventional array antenna beam pattern synthesis. Fig. 1 shows a uniform distribution of elements of the $M \times N$ array in the Cartesian coordinates system. The elements are located at $(x_m, y_n)$ on the $xy$-plane, $x_m = [m - (M+1)/2] \cdot d_x$ and $y_n = [n - (N+1)/2] \cdot d_y$, separated by $d_x$ and $d_y$ distance along the $x$ and $y$-axis, respectively. Then, the beam angle $(\theta_{Az}, \theta_{El})$ is expressed in the radar coordinates, *Az/El* coordinates having a $y$-axis pole, when the antenna's boresight is in the $+z$ direction [19]. The *Az/El* coordinate system offers a more intuitive representation of beam steering, especially for single-axis control, compared to the spherical coordinate system.

The distance $r_{mn}$ of each antenna element to the point $(r,\theta_{Az}, \theta_{El})$ where AF is to be calculated, which is a distance $r$ from the origin, is expressed as $r_{mn} = [(x_m - r\cos\theta_{El}\sin\theta_{Az})^2 + (y_m - r\sin\theta_{El})^2 + (r\cos\theta_{El}\cos\theta_{Az})^2]^{1/2}$. If that point is inside the Fraunhofer zone, then $r_{mn}$ simply abbreviated as $r - [x_m\cos\theta_{El}\sin\theta_{Az} + y_n\sin\theta_{El}]$ and the phase $\Phi_{mn} = [2\pi/\lambda_0] \cdot [x_m\cos\theta_{El}\sin\theta_{Az} + y_n\sin\theta_{El}]$, respectively. $\lambda_0$ is the free-space wavelength corresponding

to the operating frequency. The phase required for each element to steer the beam towards $(\theta_{Az,0}, \theta_{El,0})$ is given by $\Phi_0 = [2\pi/\lambda_0] \cdot \left[x_m \cos\theta_{El,0} \sin\theta_{Az,0} + y_n \sin\theta_{El,0}\right]$. In this condition, the conventional AF is calculated as shown in (1).

$$\begin{aligned} AF\,(\theta_{Az}, \theta_{El}) &= \sum_{n=1}^{N}\sum_{m=1}^{M} w_{mn} \cdot e^{j(\Phi_{mn}-\Phi_0)} \\ &= \sum_{n=1}^{N}\sum_{m=1}^{M}\Bigg[w_{mn} \cdot e^{j\frac{2\pi}{\lambda_0}(x_m \cos\theta_{El} \sin\theta_{Az}+y_n \sin\theta_{El})} \\ &\quad \cdot e^{-j\frac{2\pi}{\lambda_0}(x_m \cos\theta_{El,0} \sin\theta_{Az,0}+y_n \sin\theta_{El,0})}\Bigg] \end{aligned} \tag{1}$$

$w_{mn}$ is the magnitude (square root of power) weight of each element from input feeding with values from 0 to 1. To ensure constant total power, the $w_{mn}$ values are normalized based on the sum of the squares of the weights.

The directivity pattern of AF ($DP_{AF}$) are expressed as $U(\theta_{Az}, \theta_{El})/U_0$ where the radiation intensity is $U(\theta_{Az}, \theta_{El}) = [AF\,(\theta_{Az}, \theta_{El})]^2/2\eta_0$ and average radiation intensity is $U_0 = \left[\int_{-\pi}^{\pi}\int_{-\pi/2}^{\pi/2} U\,(\theta_{Az}, \theta_{El}) \cos\theta_{El} d\theta_{El} d\theta_{Az}\right]/4\pi$ ($\eta_0$ is free space impedance). As a result, the conventional beam pattern ($GP$; gain pattern) of array is calculated as in (2) by introducing element pattern ($EP$) to (1).

$$GP\,(\theta_{Az}, \theta_{El}) = \sum_{n=1}^{N}\sum_{m=1}^{M}\left[w_{mn} \cdot e^{j(\Phi_{mn}-\Phi_0)} \cdot EP_{mn}\,(\theta_{Az}, \theta_{El})\right] \tag{2}$$

If all element patterns are identical, (2) can be simplified to (3) [20].

$$GP\,(\theta_{Az}, \theta_{El}) = EP\,(\theta_{Az}, \theta_{El}) \cdot AF\,(\theta_{Az}, \theta_{El}) \tag{3}$$

Fig. 2 shows a near-field measurement environment and unit cell structure of the proposed transmitarray to be modeled for accurate beam pattern synthesis. In the near-field measurement environment shown in Fig. 2(a), a transmitarray is positioned in the Fresnel zone from the feeding antenna, and the radiated beam from the transmitarray is captured by the probe. Those two ports of the vector network analyzer (VNA) are connected to the feeding antenna and the probe, respectively. Since the results of the near-field measurements are obtained by signal processing of the data measured by VNA, any uncalibrated factors influence the beam pattern synthesis calculation. Therefore, in order to accurately calculate the beam pattern of the transmitarray antenna, it is imperative to identify the losses occurring between the two ports of VNA. These losses include the radiation loss of the feeding antenna, the spillover and taper losses between the feed antenna and the transmitarray, as well as the radiation loss of the transmitarray. The probe factor is excluded from the calculation as it is typically pre-calibrated within the measurement setup. The radiation loss of the transmitarray is modeled to reflect the designed unit cell characteristics as shown in Fig. 2(b). The miniaturized unit cell of the

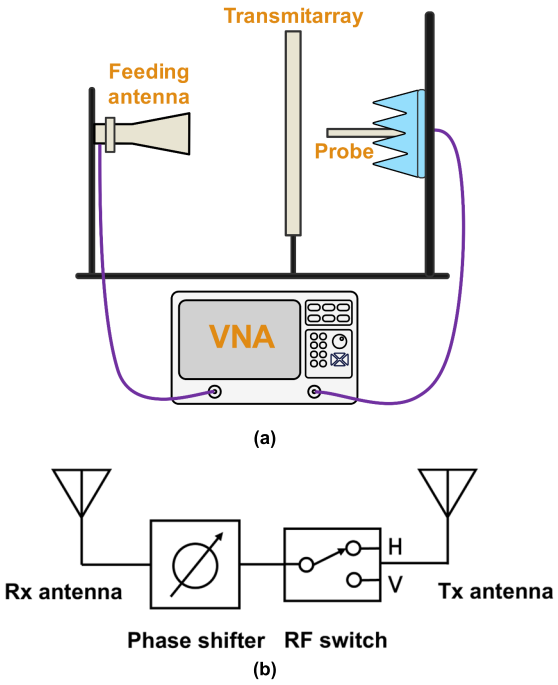


**FIGURE 2.** Factors that are modeled for accurate beam pattern synthesis: (a) near-field measurement environment and (b) a block diagram of the transmitarray's unit cell.

proposed transmitarray antenna consists of receiving (Rx) and transmitting (Tx) antennas, reflection-type phase shifter, and single pole double throw (SPDT) Positive-Intrinsic-Negative (PIN) diode switch. The reflection-type phase shifter adjusts the phase of the RF signal received from the Rx antenna to the appropriate phase for beam steering, and the SPDT PIN diode switch selects horizontal (H-pol) or vertical (V-pol) polarization of the radiated signal through the Tx antenna [21].

These modeled factors should be integrated into (1)-(3). By incorporating these factors as loss weight parameters within (1) and (2), it yields $w_{mn} = w_{feed} \times w_{spill} \times w_{mn,input} \times w_{mn,UL}$, which represents the product of multiple loss weights. As a result, the AF from (1) can be re-written as (4), denoted as $AF_{TA}$.

$$AF_{TA}\,(\theta_{Az}, \theta_{El}) = w_{spill} \cdot \sum_{n=1}^{N}\sum_{m=1}^{M} w_{mn,input} \cdot w_{mn,UL} \cdot e^{j(\Phi_{mn}-\Phi_0)} \tag{4}$$

Here, $w_{mn,input}$ is the magnitude (square root of power) weight that the Rx antenna of transmitarray receives from the feeding antenna, which is typically normalized tapered weight ($w_{mn,taper}$) in the Fresnel zone. Since $w_{mn,input}$ already incorporates the characteristics of the Rx antenna in the form of the received power, the beam pattern of the Rx antenna under the Fraunhofer field condition is neglected. $w_{spill}$ is spillover efficiency between the feeding antenna and transmitarray. The data for parameters $w_{spill}$ and $w_{mn,taper}$ are obtained by calculating the power of an area the size

of the transmitarray from the feeding antenna simulation, in which case the radiation efficiency of the feeding antenna is included in $w_{spill}$. The unit cell of certain transmitarray antennas, such as frequency selective surface (FSS), metamaterial, and receiver-transmitter structures, which do not include amplifiers, can be modeled using the proposed loss weighting $w_{mn,UL}$. This loss weighting accounts for losses arising from various components within the unit cell. When applied to the unit cell structure of Fig. 2(b), it can be defined as $w_{mn,UL} = w_{UL\_Rx} \times w_{mn,UL\_PS} \times w_{UL\_SW} \times w_{UL\_Tx}$. The spillover efficiency value, $w_{spill}$, remains constant in (4). The loss of each component can be obtained through individual element measurements. Likewise, each loss parameter can be considered as a constant value if applicable to all antenna elements uniformly. Data acquisition and comprehensive calculations for each parameter will be detailed in Section III.

The beam pattern of the transmitarray ($GP_{TA}$), as expressed in (5), is obtained by substituting the AF derived in (4) into (3) and utilizing the beam pattern of the Tx radiator as the element pattern ($EP_{Tx}$). The beam pattern of the Tx radiator is acquired via an infinite array simulation.

$$GP_{TA}(\theta_{Az}, \theta_{El}) = EP_{Tx}(\theta_{Az}, \theta_{El}) \cdot AF_{TA}(\theta_{Az}, \theta_{El})|_{w_{mn,input}=w_{mn,taper}} \quad (5)$$

Utilizing Equation (5), taper efficiency ($\varepsilon_{taper}$) is determined by comparing the peak gain with taper-weighted AF ($AF_{TA}|_{w_{mn,input}=w_{mn,taper}}$) to that with uniform-weighted AF ($AF_{TA}|_{w_{mn,input}=w_{mn,uniform}}$). To include the taper efficiency in the total efficiency ($\varepsilon_{total}$) computation, the directivity pattern of the transmitarray ($DP_{TA}$) is calculated leveraging the normalized uniform-weighted AF described in (1), and this is shown in (6).

$$DP_{TA}(\theta_{Az}, \theta_{El}) = EP_{Tx}(\theta_{Az}, \theta_{El}) \cdot AF(\theta_{Az}, \theta_{El})|_{w_{mn}=w_{mn,unifrom}} \quad (6)$$

As a result, the total efficiency of the transmitarray is expressed as (7).

$$\varepsilon_{total} = GP_{TA,max}/DP_{TA,max} \quad (7)$$

## III. UNIT CELL DESIGN AND ANTENNA SIMULATIONS FOR BEAM PATTERN SYNTHESIS

### A. MINIATURERIZED UNIT CELL DESIGN AND MEASUREMENT

Fig. 3 shows a block diagram and PCB stack-up of the unit cell structure. The unit cell of the proposed transmitarray is designed to cover a 3.3 % fractional frequency bandwidth (BW = 100 MHz) in S-band. Fabrication of the unit cell utilized RF35, a low-loss substrate characterized by $\varepsilon_r = 3.5$ and $\tan\delta = 0.0018$, enabling miniaturization with dimensions of $0.4\lambda_0 \times 0.4\lambda_0$. Further details on the miniaturization size analysis will be provided in Section III-B.

The Rx and Tx antennas operating in the S-band are designed as coupled-fed stacked patch antennas because of their low profile and high gain properties. The coupled-fed stacked patch antenna without an air gap or cavity is designed to reduce the mutual coupling between the antennas (or unit cells) because the proposed transmitarray antenna already has a miniaturized unit cell size of $0.4\lambda_0 \times 0.4\lambda_0$. This is because the coupled-fed stacked patch antenna structure confines EM fields within the stacked patches and the feeding probe. The coupling between the feeding horn antenna (source) and Rx antenna array is one of the most critical parameters since the transmitarray antenna directly receives a signal from a feeding antenna. Therefore, each Rx antenna element should have high gain radiation pattern and matched polarization to the feeding antenna.

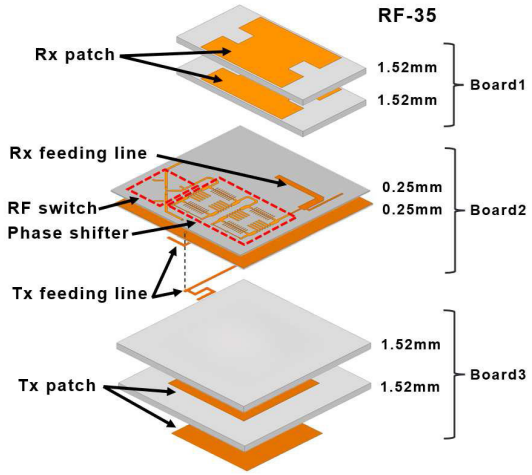


**FIGURE 3.** Proposed miniaturized transmitarray unit cell structure.

Fig. 4(a) shows the layout of the proposed coupled-fed stacked Rx and Tx antennas. There are two main differences between the Rx and Tx antennas. First, the Rx antenna occupies half of a $0.4\lambda_0 \times 0.4\lambda_0$ (width×length) unit cell's top area while the rest is allocated to the reflection-type phase shifter and the SPDT PIN diode switch. The H-shape patch of the Rx antenna improves cross-polarization suppression level and impedance matching within that area. The Tx antenna, on the other hand, has a square-shaped patch to excite two orthogonal $TM_{10}$ and $TM_{01}$ modes for dual-polarization capability, and it occupies most of the unit cell area. Second, the Rx antenna has a single vertical linear polarization that matches the polarization of the feeding antenna. The Tx antenna has a dual-polarization capability to control the polarization of the transmitted EM waves. As shown in the reflection coefficients of input ports in Fig. 4(b), the H-shape patch of Rx has improved impedance matching at the center frequency compared to the rectangular patch. The Tx and Rx antennas operate within a 100 MHz bandwidth around the center frequency. To investigate the performance of a single antenna element within an infinite array, periodic boundary conditions were employed, as illustrated in Fig. 5(a). Simulations, as shown in Fig. 5(b), indicate that both the Rx and Tx antennas

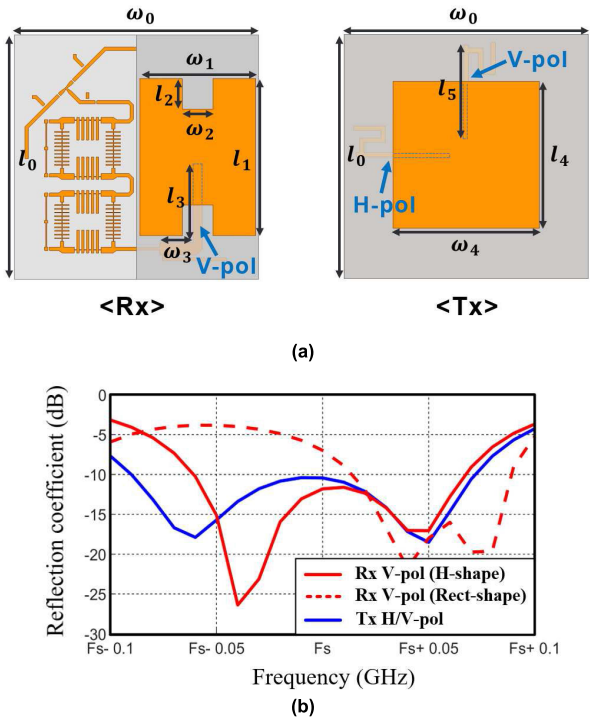


**FIGURE 4.** Coupled-fed stacked patch antennas for Rx and Tx: (a) layout and (b) reflection coefficients; $\omega_0 = 40$ mm, $\omega_1 = 19$ mm, $\omega_2 = 5$ mm, $\omega_3 = 5.5$ mm, $\omega_4 = 24$ mm, $l_0 = 40$ mm, $l_1 = 25.75$ mm, $l_2 = 5$ mm, $l_3 = 12.75$ mm, $l_4 = 24$ mm, $l_5 = 16.5$ mm.

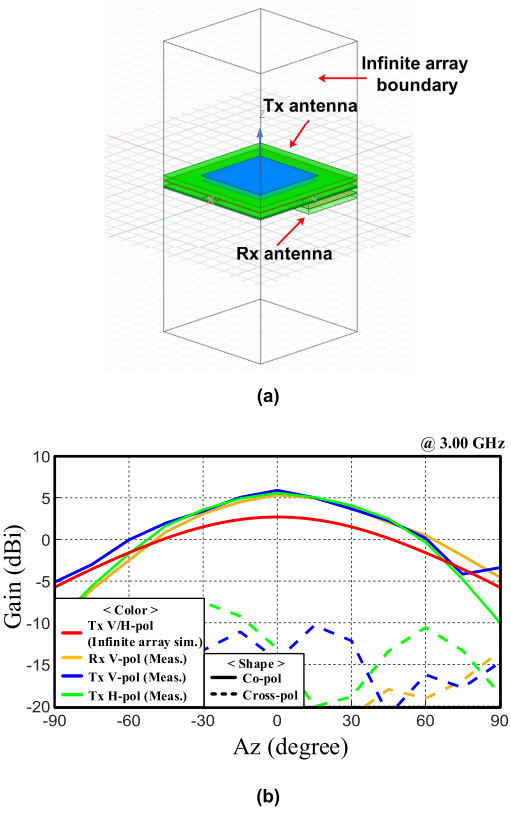


**FIGURE 5.** Antenna simulation setup and measurements for Rx and Tx: (a) finite array simulation and (b) radiation patterns.

achieve beamwidths of approximately 100° and peak gains of 2.8 dBi and 2.7 dBi, respectively. The radiation efficiency values of the Tx and Rx antennas are 74 % ($w_{UL\_Tx}$) and 69 % ($w_{UL\_Rx}$), respectively. The obtained Tx antenna beam pattern in the infinite array condition is then used as the $EP_{Tx}$ parameter in (5).

Fig. 6 shows the circuit diagram of the proposed SPDT PIN diode switch [21]. The anodes of both diodes of the proposed SPDT PIN diode are connected in common and each cathode is connected to DC bias lines for controlling forward or reverse bias. The +1.4 V bias voltage is applied for forward bias and the −5 V reverse bias voltage is applied. This voltage bias configuration can accept up to 23 dBm of RF power without affecting the PIN diode DC bias because the peak-to-peak voltage swing of 23 dBm RF power on a 50 Ω transmission line is less than the reverse bias voltage. The measured return loss (RL) values of the PIN diode switch were more than 15 dB at the operation frequency band, while the insertion loss (IL) remained below 0.9 dB ($w_{UL\_SW}$) within the operating frequency band.

This paper employs analog phase shifting which offers advantages in reducing phase quantization error for antenna gain enhancement and achieving high beamforming resolution compared to digital methods. Fig. 7 and 8 show the circuit diagrams and performance of miniaturized analog reflection-type phase shifters with one- and two-stage, respectively. The miniaturized phase shifters share the same principles as a conventional reflection-type phase and

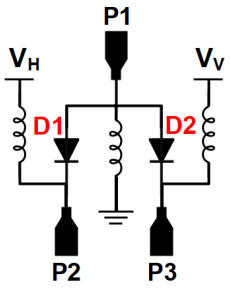


**FIGURE 6.** Circuit diagram of the proposed SPDT PIN diode switch for high RF input power and polarization selection.

comprise a hybrid coupler and reactive loads connected to the output ports of the hybrid coupler. The hybrid coupler part was miniaturized by replacing quarter-wavelength ($\lambda_g/4$) branch lines with a transmission line having slow-wave characteristics to implement the phase shifting and polarization selection switching circuits in an area of $0.2\lambda_0 \times 0.4\lambda_0$ [21] and [22]. The miniaturized coupler has only 36.7 % area ($0.08\lambda_0 \times 0.09\lambda_0$) of the conventional hybrid couplers ($0.14\lambda_0 \times 0.14\lambda_0$) on the same substrate.

Comparing the one- and two-stage phase shifters, the one-stage phase shifter shown in Fig. 7 has extra reactive loads composed of a 25 Ω quarter-wavelength transmission line and additional varactor diodes connected to it,

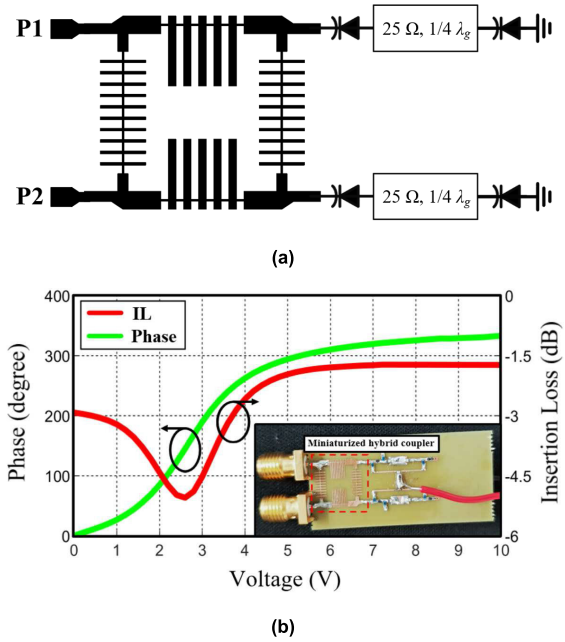


**FIGURE 7.** The one-stage analog phase shifter: (a) circuit diagram and (b) relative phase shift and IL according to a DC bias voltage.

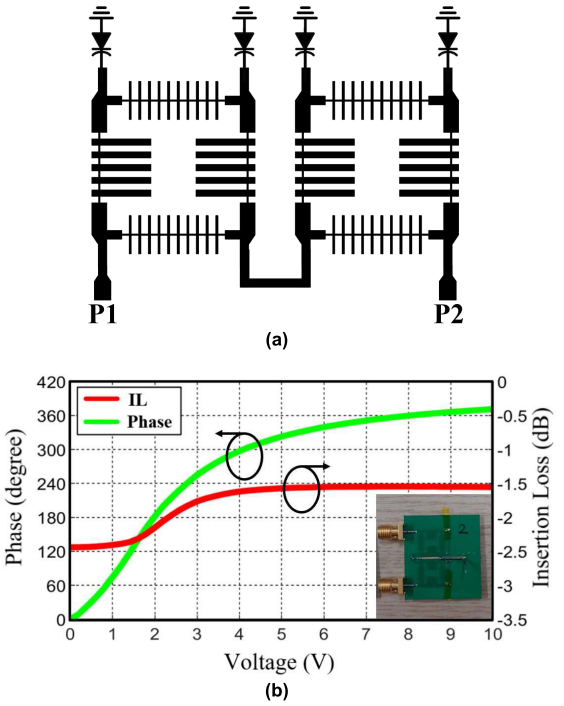


**FIGURE 8.** The two-stage analog phase shifter: (a) circuit diagram and (b) relative phase shift and IL according to a DC bias voltage.

enhancing the load impedance variation range [23]. The additional tunable loading extends the phase shifting to allow from 0 to 330°. However, it resulted in a high IL range of 1.8 ∼ 5.5 dB over applied DC voltage due to the increased parasitic elements for the added DC blocks and RF chokes to configure the bias line and the nonlinearity of the additional varactor diodes. Also, from a fabrication standpoint, they render the PCB layout more intricate, complicating the optimization design process [24]. On the other hand, the two-stage phase shifter, as illustrated in Fig. 8(a), achieves a broad phase shifting range by cascading simpler single-stage phase shifters with basic loads. Fig. 8(b) shows the measured phase shifting and IL loss results of two-stage phase shifter. Owing to its simple loading configuration, the two-stage phase shifter can phase shift over a wider 0 ∼ 360° range with a lower IL of 1.5 ∼ 2.5 dB than the one-stage. These results demonstrate that the two-stage design represents an improvement over the one-stage approach. Both miniaturized phase shifters require a 10 mV control voltage resolution for 1° phase shifting control, enabling them to significantly reduce the phase error generated by the digital phase shifting method.

Fig. 9 illustrates the loss weightings ($w_{mn,UL\_PS}$) corresponding to the phase distributions for the 8 × 8 array under beam steering conditions. Based on the measurements Fig. 8(b), the original phase values are replaced with loss weighting parameters that quantify the actual loss experienced by each cell. The overall phase distribution assigned to each unit cell is then calculated by combining two components: a compensated phase term obtained from the feed antenna simulation described in Section III-B, and a beam steering phase offset applied to each unit cell. These loss weighting of each unit cell are numerically represented at their corresponding locations within the grid. A color gradient is used in the figure, where red indicates low phase values (corresponding to high loss) and blue indicates high phase values (corresponding to low loss). Fig. 9(a) depicts the compensated phase, which accounts for the variations in loss across each unit cell relative to a reference phase of 0° set at the central cell. Fig. 9(b)-(d) show the final phase distributions obtained by adding the beam steering phase offset ($\Phi_o$) for each unit cell, corresponding to the desired beam steering angle.

Based on the unit cell measurements above, $w_{mn,UL}$ is calculated by assigning values to each of $w_{UL\_Rx}$, $w_{mn,UL\_PS}$, $w_{UL\_SW}$, and $w_{UL_Tx}$parameters. Apart from the loss associated with the phase shifter, the other loss weights remain consistent across all unit cells and can thus be regarded as constant values.

### B. EFFECT OF FEEDING ANTENNA

The tapered weighting ($w_{mn,taper}$) and spillover loss ($w_{spill}$) parameters can be efficiently obtained through simulations of a single feeding antenna. As shown in Fig. 10(a), a simulation setup was created for a $3.2\lambda_0 \times 3.2\lambda_0$ (8 × 8 array) aperture under near-field conditions (210 mm focal length, F/D = 0.46). An 11 dBi horn antenna at *S*-band (LB-284-10-C-NF, A-info [25]) served as the feeding antenna in this simulation. The simulation facilitates the extraction of data for both $w_{mn,taper}$ and $w_{spil}$parameters. $w_{spil}$ is −0.7 dB, with an average power of 0.853 W reaching the 8 × 8 array aperture

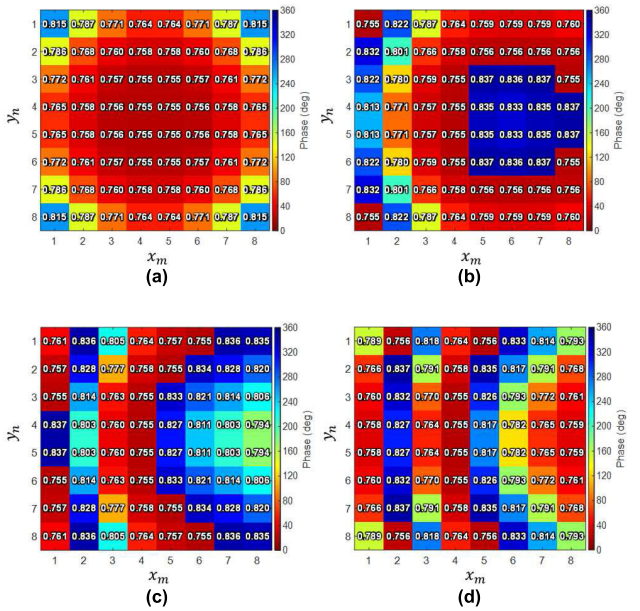


**FIGURE 9.** Insertion loss ($w_{mn,UL\_PS}$) corresponding to the phase distributions at beam steering angle ($\theta_{Az}$, $\theta_{El}$): (a) (0, 0), (b) (15, 0), (c) (30, 0), and (d) (40, 0).

for a feeding antenna input power of 1 W. It is noteworthy that this aperture power includes the radiation loss of the feeding antenna. The right-hand plot of Fig. 10(b) depicts the tapered magnitude weighting (square root of power) extracted from the feeding antenna simulation, and that the phase data used in Figure 9(a) was also obtained from the same simulation. The taper efficiency ($\varepsilon_{taper}$) is calculated using (5) by substituting the uniform weighting ($w_{mn,uniform}$) shown in the left-hand plot of Fig. 10(b) with the tapered weighting, where both weightings are normalized in terms of power.

Utilizing the derived weighting and phase data from single feeding antenna simulations in equation (1) enables the prediction of array performances, such as directivity and beamwidth. This prediction is achieved through the analysis of directivity pattern of AF ($DP_{AF}$) resulting from array size miniaturization. As an example, Fig. 10(c) illustrates the beamwidth and directivity for an 8 × 8 array antenna. This figure demonstrates the trade-off between beamwidth and directivity depending on the array spacing ($d_x$ and $d_y$ depicted in Fig. 1), which aligns with the principles of aperture antenna theory. Given the complexities of miniaturizing unit cell components and the inherent coupling effects of patch antennas, analysis reveals a unit cell spacing of $0.4\lambda_o$ as the optimal minimized unit cell size. This spacing achieves a significant reduction in physical area without substantially diminishing directivity relative to a $0.5\lambda_o$ spacing. With non-uniform weighting ($w_{mn,taper}$) and a $0.4\lambda_o$ spacing, the beamwidth and peak directivity are observed to be 18.5° and 17.25 dB, respectively. This represents a beamwidth increase of 2.5° and a directivity decrease of 2.0 dB in comparison to configurations utilizing a unit cell size of $0.5\lambda_o$.

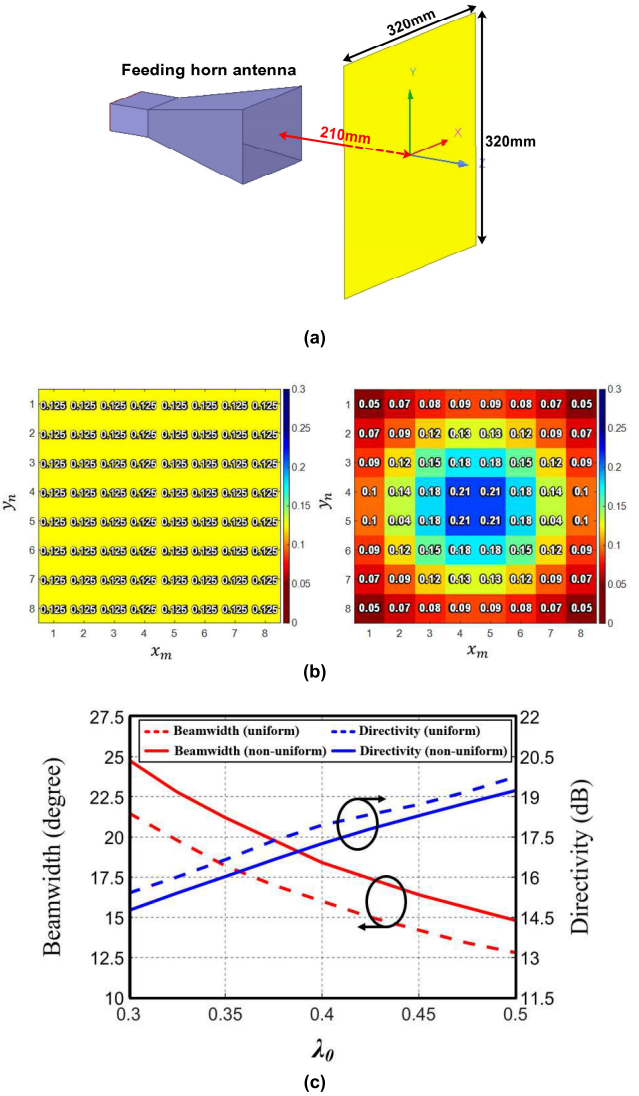


**FIGURE 10.** Feeding antenna simulation: (a) 3D modeling, (b) distributions of normalized input weighting ($w_{mn,input}$); uniform weighting $w_{mn,uniform}$ (left) and tapered weighting $w_{mn,taper}$ (right), and (c) beamwidth and directivity according to unit cell spacing ($d_x = d_y = \lambda_0$).

## IV. 8 × 8 TRANSMITARRAY BEAM PATTERN VERIFICATION

### A. ANTENNA FABRICATION AND MEASUREMENT SETUP

Fig. 11 shows the 8 × 8 transmitarray prototype and near-field measurement setup. The 8 × 8 transmitarray is fabricated from three separate printed circuit boards (PCBs) to facilitate modular assembly, as shown in Fig. 3. The rectangular patch of Rx radiator is printed on board 1, while the square patch of Tx radiator is printed on board 3. The middle layer (board 2) contains miniaturized RF circuits and feed lines for both the Rx and Tx antennas. It features 64 unit cells, along with DC control lines for the analog phase shifters and SPDT switches. The board 2 has a size of 500 mm × 420 mm × 0.5 mm (width × length × thickness). The three boards are securely fastened together using nylon bolts and nuts, resulting in a total assembled thickness of 6.88 mm.

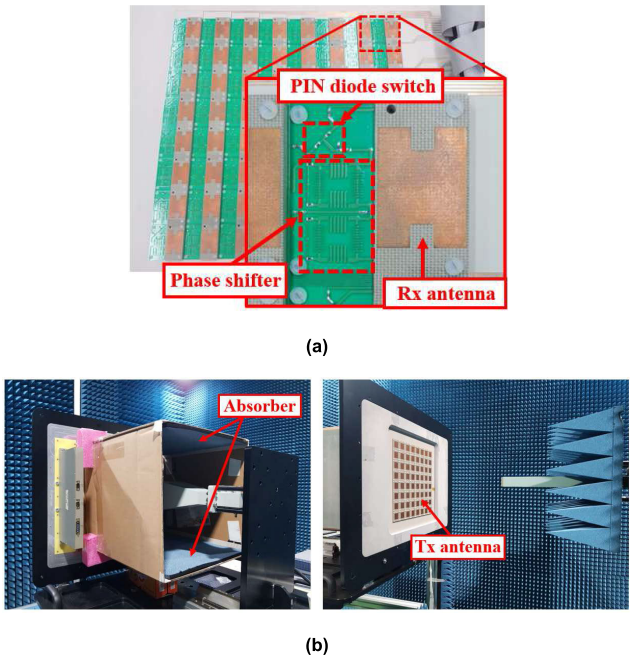


**FIGURE 11.** 8 × 8 Transmitarray measurement: (a) Fabricated transmitarray prototype and (b) near-field measurement setup.

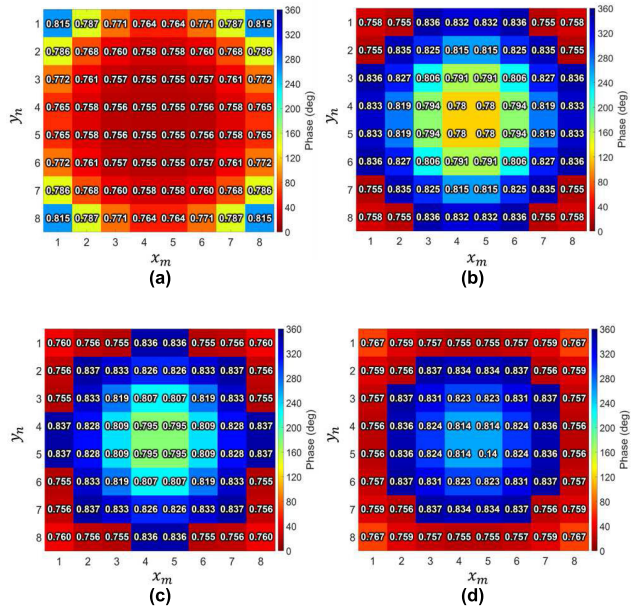


**FIGURE 12.** Phase distributions for compensation: (a) 0° offset, (b) 180° offset, (c) 210° offset, and (d) 250° offset.

The proposed 8 × 8 transmitarray antenna was measured in a near-field anechoic chamber, which is more suitable for the measurement of transmitarray or reflectarray antennas compared to far-field chambers as shown in Fig. 11(b). The performance characteristics of the fabricated 8 × 8 transmitarray antenna were rigorously evaluated through measurements conducted in an anechoic chamber, using a near-field probing technique. Commercial EM absorbers

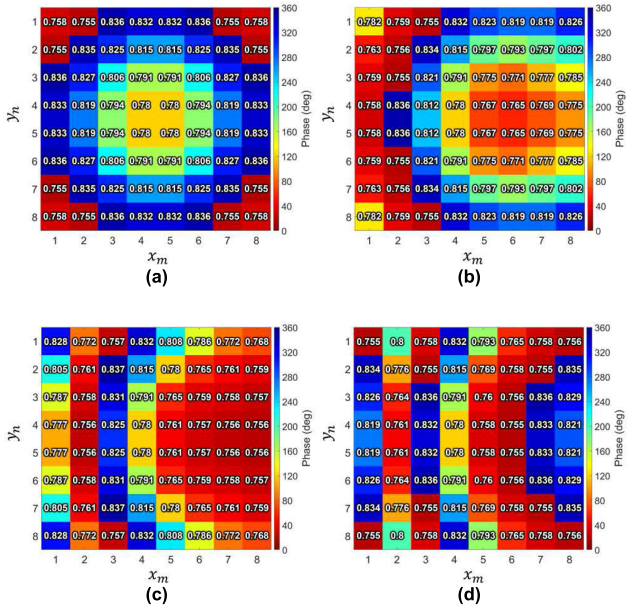


**FIGURE 13.** Optimized insertion loss ($w_{mn,UL\_PS}$) and phase distributions of phase shifter at beam steering angle ($\theta_{Az}$, $\theta_{El}$) with 180-degree offset: (a) (0, 0), (b) (15, 0), (c) (30, 0), and (d) (40, 0).

were placed on both the top and bottom sides of the feeding system to mitigate the coupling effect between the feeding antenna and the metal table supporting the transmitarray antenna. The feeding antenna was positioned 210 mm away from the receiving surface of the transmitarray antenna, resulting in a focal length ratio (F/D ratio) of 0.46. The DC voltage control board applies a +1.4 V forward bias for PIN diodes of SPDT RF switches to the activated polarization control line for polarization conversion and a −5 V reverse bias to the deactivated polarization control line. Additionally, it applies a varactor diode of the phase shifter's reverse bias of 0 to 10 V to adjust the phase value of each unit cell as needed. The designed transmitarray antenna needs a DC power of less than 2.5 W for beam steering and polarization control. This is due to the majority of the diodes operating with reverse bias current, with only 64 PIN diodes requiring a forward bias current.

### *B. PEAK GAIN OPTIMIZATION AND EXPERIMENTAL RESULT*

To maximize the peak gain of the transmitarray, the phase compensation values are strategically adjusted through the addition of phase offsets. This optimization ensures that the resulting phase distribution falls within the phase range exhibiting minimal IL according to the performance of the employed analog phase shifter, as shown in Fig. 8. Fig. 12 presents the phase distribution after adding phase offsets of 0°, 180°, 210°, and 250° to the initial phase distribution from Fig. 9(a). Notably, the region with the lowest loss (depicted in blue) exhibits the widest distribution in Fig. 12(b). Table 1 summarizes the measured peak antenna gain and radiation

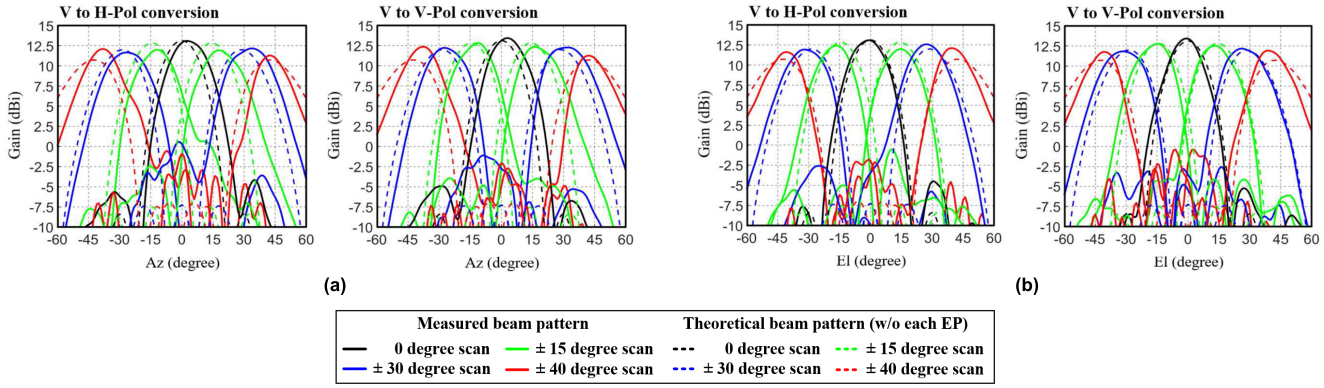


**FIGURE 14.** 2D beam steering patterns (V-to-H-pol or V-to-V-pol): (a) azimuth and (b) elevation angles (rectangular plot).

**TABLE 1.** The peak gain and radiation efficiency.

| Offset (deg) | 0 | 180 | 210 | 250 |
|---|---|---|---|---|
| Calculated gain (dBi) | 13.1 | 13.6 | 13.6 | 13.5 |
| Calculated radiation loss (dB) | 7.5 | 7.1 | 7.1 | 7.1 |
| Measured gain (dBi) | 12.1 | 13.3 | 13.1 | 12.7 |
| Measured radiation loss (dB) | 7.8 | 6.8 | 6.9 | 7.2 |

**TABLE 2.** 8 × 8 Transmitarray parameters.

| Parameter type (symbol) | | Value | Data Source |
|---|---|---|---|
| Taper loss ($\varepsilon_{taper}$) | | 0.7 dB | Cal. |
| Spillover loss ($w_{spill}$) | | 0.7 dB | Sim. |
| Unit cell loss ($w_{mn,UL}$) | Rx antenna loss ($w_{UL\_Rx}$) | 1.6 dB | Meas. |
| | Average phase shifter loss ($w_{mn,UL\_PS}$) | 1.9 dB | Meas. |
| | PIN diode switch loss ($w_{UL\_SW}$) | 0.9 dB | Meas. |
| | Tx antenna loss ($w_{UL\_Tx}$) | 1.3 dB | Meas. |
| Total loss ($\varepsilon_{total}$) | | 7.1 dB | Cal. |
| Element pattern of Tx ($EP_{Tx}$) | | 2.7 dBi | Sim. |

*Sim.: Simulation, Meas.: Measurement, Cal.: Calculation

efficiency values at the center frequency for each phase offset. The highest gain of 13.3 dBi and radiation efficiency of 20.8% were achieved at a phase offset of 180°. By comparing the calculated beam synthesis results (using equations from Section II) with the measured data from Section III, a close agreement is observed between the calculated and measured peak gain and total loss values, with a deviation of less than 1 dB. Based on the measured results, the 180° offset is chosen as the optimal value for beam steering applications. This offset is then added to the phase values corresponding to pre-defined beam steering angles of $(\theta_{Az}, \theta_{El}) = (0, 0)$, (15, 0), (30, 0), and (45, 0) beam steering angles. The resulting $w_{mn,UL\_PS}$ for these beam steering angles are illustrated in Fig. 13.

By substituting the previously defined parameters into (5) to (7), the calculated beam pattern exhibits peak gain and directivity of 13.6 dBi and 20.7 dBi, respectively, at the central beam steering angle. Utilizing (5) and comparing the taper-weighted peak gain with the uniform-weighted counterpart in Fig. 10(b), the taper efficiency ($\varepsilon_{taper}$) is determined to be −0.7 dB. Equation (7) is then employed to calculate the total efficiency, yielding a value of −7.1 dB. These loss parameters, summarized in Table 2, represent the cumulative loss experienced by the transmitarray and serve as an analytical tool for evaluating the performance of the fabricated transmitarray. Fig. 14 compares the measured and calculated steered beam patterns for various azimuth ($Az$) and elevation ($El$) angles at the center frequency. These comparisons are presented as rectangular plots for both V-to-H-polarization (V-to-H-pol) and V-to-V-polarization (V-to-V-pol) conversions. The steerable beam achieved a range of +/- 40° in both azimuth and elevation planes. Beam widths measured at steering angles of 0°, 15°, 30°, and 40° were 18°, 17°, 23°, and 11°, respectively. The corresponding gains were observed to be approximately 13 dB, 12.5 dB, 12 dB, and 12 dB. The directivity exhibited minor fluctuations between 19.5 and 20 dBi, likely due to variations in loss at different steering angles. The sidelobe suppression level was approximately 15 dB. The total measured efficiency was −6.8 dB, and the measured aperture efficiency was 17.8%.

Fig. 15 presents the theoretical and measured beam patterns in polar plots, facilitating a clear visualization of their shape variations. The theoretical pattern, denoted by circled dots, closely aligns with the measured pattern (solid line) considering fabrication errors. However, a discrepancy is observed at +/- 40° beam steering. This discrepancy arises from a difference in element patterns. The theoretical model assumes an ideal infinite array, where all elements experience identical coupling environments. In contrast, the actual element pattern on the edge of the 8 × 8 array experiences distinct coupling effects compared to the surrounded elements due to the absence of neighboring elements on one or more sides.

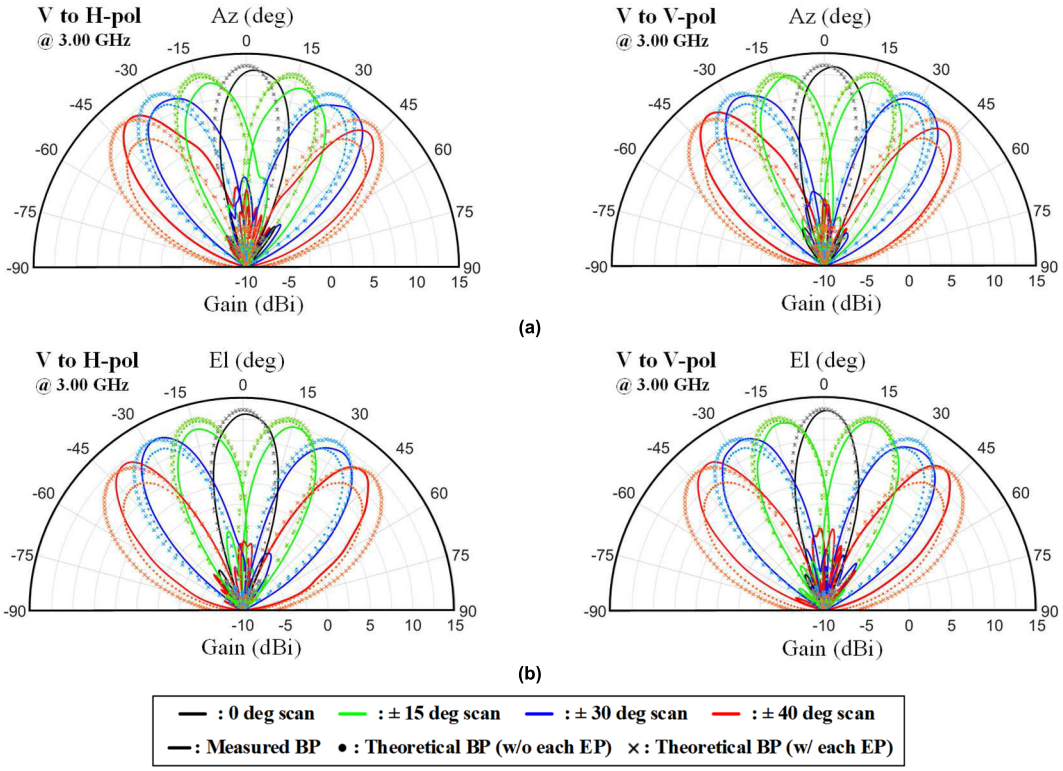


**FIGURE 15.** 2D beam steering patterns (V-to-H-pol or V-to-V-pol): (a) azimuth and (b) elevation angles.

**TABLE 3.** Performance comparison between the proposed 8 × 8 and literature-reported transmitarray antennas.

| Ref. | Freq. Band | Unit Cell Size | Phase Shifting Method | Beam Steering Angle | Aperture efficiency | Pol. Conv. | Array Size |
|---|---|---|---|---|---|---|---|
| [26] | C | $0.48\lambda_0 \times 0.48\lambda_0$ | 0 ~ 360° (Analog) | +/-60° | 27 % | LP→LP/CP | 8 × 8 |
| [27] | X | $0.47\lambda_0 \times 0.47\lambda_0$ | 1-bit (Digital) | n/a | n/a | LP→CP | 8 × 8 |
| [28] | Ka | $0.46\lambda_0 \times 0.46\lambda_0$ | 2-bit (Digital) | +/-60° | 11.3 % | LP→CP | 20 × 20 |
| [6] | X | $0.47\lambda_0 \times 0.47\lambda_0$ | 1-bit (Digital) | +/-15° | n/a | LP→LP | 4 × 4 |
| previous research [21] | **S** | **$0.4\lambda_0 \times 0.4\lambda_0$** | **0 ~ 360° (Analog)** | **+/-40°** | 4.3 % | **LP→LP** | **8 × 8** |
| **This research** | | | | | **17.8 %** | | |

This lack of neighboring elements leads to reduced mutual coupling, increased edge effects, and a modified radiation pattern for the edge elements. This is confirmed by the fact that the cross-marked beam pattern computed using finite array EM simulation, which incorporates the actual element patterns of each Tx antenna, closely matches the measured beam pattern. In larger arrays, such as 16 × 16 or 32 × 32 configurations, where numerous elements share a consistent coupling environment, these discrepancies at wider angles are expected to diminish.

Table 3 shows a performance comparison with other recently reported research on transmitarrays employing a receiver-transmitter architecture. These transmitarrays share the characteristic of unit cell dimensions smaller than $0.5\lambda_0$ and offer functionalities for both polarization conversion and beam steering. Compared to prior works, the transmitarray presented in this paper achieves a minimum unit cell size of $0.4\lambda_0$. Additionally, it exhibits enhanced phase resolution, enabling precise beam steering. Building upon the advancements reported in [21], this work further refines the phase shifter performance to achieve a full 360° phase shift, thereby minimizing losses caused by phase errors. It also realizes a 13.5% improvement in aperture efficiency.

## V. CONCLUSION

This paper proposed a miniaturized 8 × 8 transmitarray antenna with a unit cell size of $0.4\lambda_0$. Each unit cell incorporates a linearly polarized transmitting and receiving antennas,

an SPDT PIN diode switch, and a two-stage miniaturized reflection-type phase shifter. Array factor analysis with accurate unit cell and measurement environment modeling was employed to calculate the theoretical beam pattern and predict the performance of the transmitarray. The fabricated transmitarray antenna successfully validated the design concept, achieving simultaneous linear polarization conversion and +/- 40° beam steering capabilities. It exhibited a measured approximately 13 dB peak gain and 17.8% aperture efficiency. The proposed beam pattern synthesis method has been verified through experimental measurements. This method allows for optimization of the phase distribution, leading to enhanced antenna gain. The miniaturization and optimization techniques discussed in this paper are scalable and can be applied to other array antenna applications for next-generation communication and radar systems.

## REFERENCES

[1] Z. Xiao, L. Zhu, Y. Liu, P. Yi, R. Zhang, X.-G. Xia, and R. Schober, "A survey on millimeter-wave beamforming enabled UAV communications and networking," *IEEE Commun. Surveys Tuts.*, vol. 24, no. 1, pp. 557–610, 1st Quart., 2022.
[2] P.-Y. Qin, L.-Z. Song, and Y. J. Guo, "Conformal transmitarrays for unmanned aerial vehicles aided 6G networks," *IEEE Commun. Mag.*, vol. 60, no. 1, pp. 14–20, Jan. 2022.
[3] R. E. Hodges, N. Chahat, D. J. Hoppe, and J. D. Vacchione, "A deployable high-gain antenna bound for mars: Developing a new folded-panel reflectarray for the first CubeSat mission to Mars," *IEEE Antennas Propag. Mag.*, vol. 59, no. 2, pp. 39–49, Apr. 2017.
[4] S. Yang, Z. Yan, M. Cai, and X. Li, "Low-profile dual-band circularly polarized antenna combining transmitarray and reflectarray for satellite communications," *IEEE Trans. Antennas Propag.*, vol. 70, no. 7, pp. 5983–5988, Jul. 2022.
[5] L. Wu, K. Lou, J. Ke, J. Liang, Z. Luo, J. Y. Dai, Q. Cheng, and T. J. Cui, "A wideband amplifying reconfigurable intelligent surface," *IEEE Trans. Antennas Propag.*, vol. 70, no. 11, pp. 10623–10631, Nov. 2022.
[6] P. Nayeri, A. Z. Elsherbeni, and F. Yang, "Radiation analysis approaches for reflectarray antennas [antenna designer's notebook]," *IEEE Antennas Propag. Mag.*, vol. 55, no. 1, pp. 127–134, Feb. 2013.
[7] P. Nayeri, F. Yang, and A. Z. Elsherbeni, *Reflectarray Antennas: Theory, Designs, and Applications*. Hoboken, NJ, USA: Wiley, 2018.
[8] L. Di Palma, A. Clemente, L. Dussopt, R. Sauleau, P. Potier, and P. Pouliguen, "Radiation pattern synthesis for monopulse radar applications with a reconfigurable transmitarray antenna," *IEEE Trans. Antennas Propag.*, vol. 64, no. 9, pp. 4148–4154, Sep. 2016.
[9] A. H. Abdelrahman, F. Yang, A. Z. Elsherbeni, P. Nayeri, and C. A. Balanis, *Analysis and Design of Transmitarray Antennas*. San Rafael, CA, USA: Morgan & Claypool, 2017.
[10] C. C. Cruz, C. A. Fernandes, S. A. Matos, and J. R. Costa, "Synthesis of shaped-beam radiation patterns at millimeter-waves using transmit arrays," *IEEE Trans. Antennas Propag.*, vol. 66, no. 8, pp. 4017–4024, Aug. 2018.
[11] S. Loredo, G. Leon, and E. G. Plaza, "A fast approach to near-field synthesis of transmitarrays," *IEEE Antennas Wireless Propag. Lett.*, vol. 20, pp. 648–652, 2021.
[12] D. R. Prado, "The generalized intersection approach for electromagnetic array antenna beam-shaping synthesis: A review," *IEEE Access*, vol. 10, pp. 87053–87068, 2022.
[13] B. Rana, I.-G. Lee, and I.-P. Hong, "Digitally reconfigurable transmitarray with beam-steering and polarization switching capabilities," *IEEE Access*, vol. 9, pp. 144140–144148, 2021.
[14] J. Tang, S. Xu, F. Yang, and M. Li, "Design and measurement of a reconfigurable transmitarray antenna with compact varactor-based phase shifters," *IEEE Antennas Wireless Propag. Lett.*, vol. 20, pp. 1998–2002, 2021.
[15] Y. Wang, S. Xu, F. Yang, and D. H. Werner, "1 bit dual-linear polarized reconfigurable transmitarray antenna using asymmetric dipole elements with parasitic bypass dipoles," *IEEE Trans. Antennas Propag.*, vol. 69, no. 2, pp. 1188–1192, Feb. 2021.
[16] Y. Xiao, F. Yang, S. Xu, M. Li, K. Zhu, and H. Sun, "Design and implementation of a wideband 1-bit transmitarray based on a Yagi–Vivaldi unit cell," *IEEE Trans. Antennas Propag.*, vol. 69, no. 7, pp. 4229–4234, Jul. 2021.
[17] H. Li, Y. B. Li, C. Y. Gong, S. Y. Dong, S. Y. Wang, H. P. Wang, and T. J. Cui, "Design of programmable transmitarray antenna with independent controls of transmission amplitude and phase," *IEEE Trans. Antennas Propag.*, vol. 70, no. 9, pp. 8086–8099, Sep. 2022.
[18] M. Wang, S. Xu, N. Hu, W. Xie, F. Yang, and Z. Chen, "A low-profile wide-angle reconfigurable transmitarray antenna using phase transforming lens with virtual focal source," *IEEE Trans. Antennas Propag.*, vol. 70, no. 9, pp. 8626–8631, Sep. 2022.
[19] A. D. Brown, *Electronically Scanned Arrays MATLAB? Modeling and Simulation*. Boca Raton, FL, USA: CRC Press, 2012.
[20] R. J. Mailloux, *Phased Array Antenna Handbook*. Norwood, MA, USA: Artech House, 2005.
[21] M. Hwang, G. Kim, J. Kim, and S. Kim, "A simultaneous beam steering and polarization converting S-band transmitarray antenna," *IEEE Access*, vol. 10, pp. 105111–105119, 2022.
[22] K.-O. Sun, S.-J. Ho, C.-C. Yen, and D. van der Weide, "A compact branch-line coupler using discontinuous microstrip lines," *IEEE Microw. Wireless Compon. Lett.*, vol. 15, no. 8, pp. 519–520, Aug. 2005.
[23] C.-S. Lin, S.-F. Chang, and W.-C. Hsiao, "A full-360° reflection-type phase shifter with constant insertion loss," *IEEE Microw. Wireless Compon. Lett.*, vol. 18, no. 2, pp. 106–108, Feb. 2008.
[24] M. Hwang, G. Kim, I.-G. Lee, and S. Kim, "Design of miniaturized 360° analog phase shifter for multi-functional transmit-array antenna," *J. Korean Inst. Electromagn. Eng. Sci.*, vol. 34, no. 2, pp. 103–110, Feb. 2023.
[25] *A-INFO, 2.60–3.95 GHz Standard Gain Horn Antenna*, Standard LB-284-65910, Nov. 2023.
[26] C. Huang, W. Pan, X. Ma, B. Zhao, J. Cui, and X. Luo, "Using reconfigurable transmitarray to achieve beam-steering and polarization manipulation applications," *IEEE Trans. Antennas Propag.*, vol. 63, no. 11, pp. 4801–4810, Nov. 2015.
[27] C. Huang, W. Pan, X. Ma, and X. Luo, "1-bit reconfigurable circularly polarized transmitarray in X-band," *IEEE Antennas Wireless Propag. Lett.*, vol. 15, pp. 448–451, 2016.
[28] L. Di Palma, A. Clemente, L. Dussopt, R. Sauleau, P. Potier, and P. Pouliguen, "Circularly-polarized reconfigurable transmitarray in Ka-band with beam scanning and polarization switching capabilities," *IEEE Trans. Antennas Propag.*, vol. 65, no. 2, pp. 529–540, Feb. 2017.

**MYEONGHA HWANG** received the B.S. degree from the Department of Electronics Engineering, Pusan National University, Busan, Republic of Korea, in 2020, where he is currently pursuing the M.S. and Ph.D. degrees. His current research interests include array antenna design and RF systems.

**GYOUNGDEUK KIM** received the B.S. degree in electronics engineering from Pusan National University, South Korea, in 2020, where he is currently pursuing the M.S. and Ph.D. degrees. His current research interests include antenna design and RF systems.

**INGON LEE** received the M.S. and Ph.D. degrees in information and communication engineering from Kongju National University, Cheonan, South Korea, in 2016 and 2020, respectively. From 2020 to 2021, he was a Postdoctoral Research Fellow with Kongju National University. Since 2021, he has been with Hanwha Systems, Yongin, South Korea, where he is currently a Senior Engineer. His research interests include periodic electromagnetic structures, microwave/millimeter-wave circuits and components, and transmitarray antenna for radar applications.

**SANGKIL KIM** (Senior Member, IEEE) received the B.S. degree (magna cum laude) from the School of Electrical and Electronics Engineering, Yonsei University, Seoul, Republic of Korea, in 2010, and the M.S. and Ph.D. degrees from the School of Electrical and Computer Engineering, Georgia Institute of Technology, GA, Atlanta, USA, in 2012 and 2014, respectively. From 2015 to 2018, he was with Qualcomm Inc., San Diego, CA, USA, as a Senior Engineer. He joined as the Faculty Member of the Department of Electronics Engineering, Pusan National University, Busan, Republic of Korea, in 2018. He has published 43 articles in peer-reviewed journals and five book chapters. His research interests include mmWave phased antenna array, machine learning assisted backscattering communication, RF biosensors, energy harvesting, and printed RF electronics. He is a member of IEEE MTT-26 RFID, Wireless Sensors, and the IoT Committee. He received the IET Premium Award for Microwave, Antennas and Propagation in 2015 and the KIEES Young Researcher Award in 2019.

**JONG-GWAN YOOK** (Senior Member, IEEE) was born in Seoul, South Korea. He received the B.S. and M.S. degrees from Yonsei University, Seoul, in 1987 and 1989, respectively, all in electronics engineering, and the Ph.D. degree from the University of Michigan, Ann Arbor, MI, USA, in 1996.

He is currently a Professor with the School of Electrical and Electronic Engineering, Yonsei University. His research team recently developed various biosensors, such as carbon-nanotube RF biosensors for nanometer-size antigen-antibody detection and remote wireless vital signal monitoring sensors. His current research interests include theoretical/numerical electromagnetic modeling and characterization of microwave/millimeter-wave circuits and components, design of radiofrequency integrated circuits (RFICs) and monolithic microwave integrated circuits (MMICs), and analysis and optimization of high-frequency highspeed interconnects, including signal/power integrity (EMI/EMC), based on frequency-and-domain full-wave methods.